Experimental Neurology 393 (2025) 115386

Contents lists available at ScienceDirect

Experimental Neurology

journal homepage: www.elsevier.com/locate/yexnr

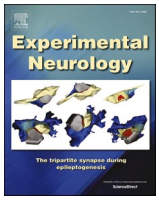

Research paper

Mapping of projection of sprouting neuron in neonate and adult mice after pyramidotomy

Hiroshi Tsujioka [a,b,*], Toshihide Yamashita [a,b,c,d,*]

[a] Graduate School of Medicine, Osaka University, Suita, Osaka, Japan
[b] WPI Immunology Frontier Research Center, Osaka University, Suita, Osaka, Japan
[c] Graduate School of Frontier Biosciences, Osaka University, Osaka, Japan
[d] Department of Neuro-Medical Science, Graduate School of Medicine, Osaka University, Suita, Osaka, Japan

ARTICLE INFO

Keywords:
MAPseq
Sprouting
Corticospinal tract
Neonate
Pyramidotomy

ABSTRACT

Although severed axons of the corticospinal tract rarely regenerate, neural function is partially recovered by axonal sprouting from intact neurons. The sprouting capability is higher in neonates than in adults, making neonates an attractive model for finding novel therapeutic targets for central nervous system injury. The axonal projection pattern of the motor cortex neurons is highly heterogeneous, and high-throughput analysis at the single-cell level is required to correctly understand the projection pattern of sprouting neurons. The recently developed multiplexed analysis of projections by sequencing (MAPseq) has revealed axonal projection complexity in many brain areas; however, axonal sprouting of the corticospinal tract in neonates and adults has not yet been analyzed. Here, we evaluated the sprouting pattern of individual neurons using MAPseq in neonate and adult mice after pyramidotomy, using the intact and denervated (sprouting) sides of the cervical cord. The ratio of neurons projecting solely to the intact or denervated side or projecting to both sides was not significantly different. The cumulative projection strength on the denervated side was significantly higher in the neonatal pyramidotomy group than in the other groups. The ratio of the projection strength on the denervated side to the total projection strength (sprouting index) correlated with the projection strength on the denervated side. The ratio of the neuron with a sprouting index of 0.6–0.7 was significantly higher in the neonatal pyramidotomy group. These results show the usefulness of MAPseq in sprouting studies and provide important information regarding the sprouting patterns of individual neurons in neonates.

1. Introduction

Injury to the central nervous system (CNS) often causes lifelong disability due to its inability to regenerate severed axons. However, axons sprouting from intact neurons form compensatory neural circuits that lead to partial functional recovery (Benowitz and Carmichael, 2010; Tsujioka and Yamashita, 2021). Axonal sprouting of the corticospinal tract (CST) is a well-studied model, since the CST is mainly responsible for voluntary movement in humans, which is important for the quality of life, or fine movement in rodents. In rodents, the cell bodies of corticospinal neurons (CSN) reside in the layer V of the cerebral cortex. The axon mainly passes through the ipsilateral side of the pyramid of medulla oblongata, pyramidal decussation, and contralateral side of the dorsal column (main CST), and makes synapses mainly on the contralateral side of the interneurons in the dorsal horn (Canty and Murphy, 2008; Welniarz et al., 2017). In human, main CST passes through lateral column, and the axons mainly innervate ventral horn. Approximately 4 weeks after ablation of the unilateral side of the CST by cortical injury or pyramidotomy, the axonal branch of the CSN grows into the denervated side of the propriospinal neurons, which accompanies partial functional recovery in mice. Since a second injury to the intact side of the CST causes relapse of paralysis by first injury, axonal sprouting is believed to be important for functional recovery (Ueno et al., 2012).

The capacity for axonal sprouting is much higher in neonates than in adults (Liu et al., 2010; Omoto et al., 2010; Tsujioka and Yamashita, 2019; Z'Graggen et al., 2000). In a pyramidotomy model, the number of axons growing into the denervated side was almost 10-fold higher when mice were injured on postnatal day 7 (P7) than when mice were injured at 2 months of age (Liu et al., 2010). A higher functional recovery of fine motor movement compared to adults after cortical injury has also been

* Corresponding authors at: 2-2, Yamadaoka, Suita, Osaka 565-0871, Japan.
E-mail addresses: tsujioka-tky@umin.org (H. Tsujioka), yamashita@molneu.med.osaka-u.ac.jp (T. Yamashita).

https://doi.org/10.1016/j.expneurol.2025.115386
Received 17 February 2025; Received in revised form 30 June 2025; Accepted 16 July 2025
Available online 17 July 2025

observed (Omoto et al., 2011). Activation of the mechanistic target of rapamycin kinase pathway, which is selectively activated in neonates, by deletion of the phosphatase and tensin homolog (PTEN) in adults causes an increase in sprouting axons after pyramidotomy, suggesting that comparison between neonates and adults is promising for finding possible therapeutic targets for CNS injury.

The axonal projection patterns of motor cortex neurons are heterogeneous (Muñoz-Castañeda et al., 2021). They can be divided into intratelencephalic, corticothalamic, and pyramidal tract (or extratelencephalic) neurons. The pyramidal tract neurons are further divided into corticobulbar neurons and CSNs (Hausmann et al., 2022). At least two types of sprouting CSNs are present in neonatal hamsters (Aisaka et al., 1999), suggesting that the axonal projection pattern of sprouting is also heterogeneous. Although revealing the heterogeneity of the projection patterns of sprouting CSNs is important for understanding the molecular mechanisms of axonal sprouting and identifying possible therapeutic targets, high-throughput analysis of axonal projections at the single-cell level has not yet been reported.

The axonal projection patterns of individual neurons can be visualized using sparse labeling (Wu et al., 2021). Brainbow or related techniques are other methods for visualizing the projection patterns of individual neurons by labeling with different colors using several types of fluorescent proteins (Cai et al., 2013; Livet et al., 2007; Sakaguchi et al., 2018). However, the throughputs of these methods are low. The recently developed multiplexed analysis of projections by sequencing (MAPseq) is an easy-to-use, high-throughput method for revealing the axonal projection patterns of individual neurons (Kebschull et al., 2016a). MAPseq is a single-cell analysis of axonal projection through infection of the barcoded Sindbis virus vector (Ehrengruber et al., 2011; Huang, 1996; Kebschull et al., 2016b) followed by the detection of barcoded RNA in the target tissue by next-generation sequencing. Green fluorescent protein (GFP) RNA, barcode RNA, and boxB sequence are transcribed under a promotor, and MAPPnλ RNA is transcribed from another promoter on the genomic RNA of the Sindbis virus. An engineered protein MAPPnλ, in which presynaptic terminal localization signal is fused with nλ RNA binding domain, is then translated. nλ domain binds to boxB sequence, therefore GFP-barcode-boxB RNA is transported to presynaptic terminals. Since expression from a Sindbis virus reaches very high level rapidly, axons of a neuron are filled with the barcode RNA. High diversity of barcode ensures uniqueness of barcode in each neuron (Kebschull et al., 2016a). It can distinguish virtually all the neurons in the mouse brain. MAPseq has revealed the complexity of projection patterns of neurons in many brain areas such as the motor cortex (Abe et al., 2024; Hausmann et al., 2022), somatosensory cortex (Abe et al., 2024), visual cortex (Abe et al., 2024; Han et al., 2018), medial prefrontal cortex (Mathis et al., 2021), olfactory cortex (Chen et al., 2022), or hippocampus (Gergues et al., 2020); however, sprouting of CSNs after brain injury has not been conducted yet.

In this study, we conducted high-throughput single-cell axonal projection mapping of the sprouting CST after pyramidotomy using MAPseq in neonates and adults. Thousands of barcodes were detected on the denervated or intact sides of the spinal cord in both neonates and adults. The ratio of neurons solely projecting to the intact, denervated side, or projecting to both sides was not significantly different after pyramidotomy in both neonates and adults. The cumulative projection strength on the denervated side (sprouting axons) was significantly higher in the neonatal pyramidotomy group than in the other groups. The ratio of sprouting axons to total axons (sprouting index) correlated with the projection strength of the sprouting axons. The ratio of neurons was significantly higher in the neonatal pyramidotomy group at a sprouting index of 0.6–0.7. These results provide important basic knowledge regarding the heterogeneity of axonal sprouting, especially in neonates.

2. Materials and methods

2.1. Animals

Female C57BL/6J wild-type mice were used in this study. The mice were maintained under a 12-h light/12-h dark cycle and fed ad libitum under specific pathogen-free conditions. All animal experiments followed a protocol approved by the Animal Experiment Committee of Osaka University (permission number 05–077). All surgical procedures were conducted under complete anesthesia using an intraperitoneal injection of medetomidine, midazolam, and butorphanol.

2.2. Surgery

Pyramidotomy was performed as described previously (Starkey et al., 2005; Tsujioka and Yamashita, 2023, 2019). Briefly, the neck was incised on the ventral side, and the medulla oblongata was injured at ~ 0.5 mm width and ~ 0.25 mm depth on the left side of the basal artery for both neonate and adult. In the sham group, the medulla oblongata was exposed but not injured. In the neonatal group, postnatal day 7 (P7) mice were injured, whereas in the adult group, mice at 8 weeks of age (8 W) were injured.

2.3. Infection of Sindbis virus

Infection with the barcoded Sindbis virus was performed as previously described (Kebschull et al., 2016a). In brief, a barcoded Sindbis virus library expressing green fluorescent protein (GFP; ~2×10^9 infectious particles/mL, estimated diversity was ~20 M) was purchased from the MAPseq/BARseq Core Facility, Cold Spring Harbor Laboratory. To label corticospinal neurons (Tsujioka and Yamashita, 2019), the virus was injected (0 mm anterior, 1 mm right), (0.5 mm anterior, 1 mm right), and (0.5 mm anterior, 1.5 mm right) from the bregma at a depth of 0.6 mm. The injection volume was 200 nL at an injection speed of 100 nL/min using NANOLITER2020 (WPI). The virus was injected 26 days after the pyramidotomy or sham surgery.

Approximately 40–44 h after injection, the spinal cord tissue at the level of the C4–7 vertebrae was harvested without perfusion, it was cut into the left and right sides, the dorsal column was removed manually, and the tissue was freshly frozen on dry ice. Tissues at the injection site were manually collected under GFP filter and freshly frozen. They were homogenized twice in TRIzol (Sigma) using Micro Smash (Tomy, MS-100R) with 1-mm diameter zirconia beads (Tomy, ZB-100) at 4000 rpm for 30 s. RNA was extracted and sequenced at the MAPseq/BARseq Core Facility. Library construction and sequencing, including how spike-in was added, is the same as the original paper. In brief, the total RNA extracted from tissue, including barcode RNA, were reverse transcribed together with a known amount of spike-in RNA, which was synthesized by in vitro transcription and quantified accurately. After reverse transcription, barcode cDNA from each brain area received a unique slice specific identifier (SSI) to be differentiated from other brain areas, and each barcode molecule received a unique molecular identifier (UMI) for quantification. The barcode amplicons were amplified by nested PCR, and pooled. The 400 M of 36 bp paired-end reads were produced from the pooled library using NextSeq500. The ratio of the injection site to the target site RNA used for sequencing was 1 to 9. Approximately, 400 M paired-end reads were obtained. The spinal cord tissue at the level of C1–3 vertebrae was also collected and fixed in 4 % paraformaldehyde (PFA)/0.1 M phosphate buffer (PB) overnight at 4 °C for histological analysis.

2.4. Histological analyses

Histological analyses were performed essentially as previously described (Tsujioka and Yamashita, 2023, 2019). Briefly, for evaluation of injection in Fig. 1D, mice injected with the Sindbis virus was perfused

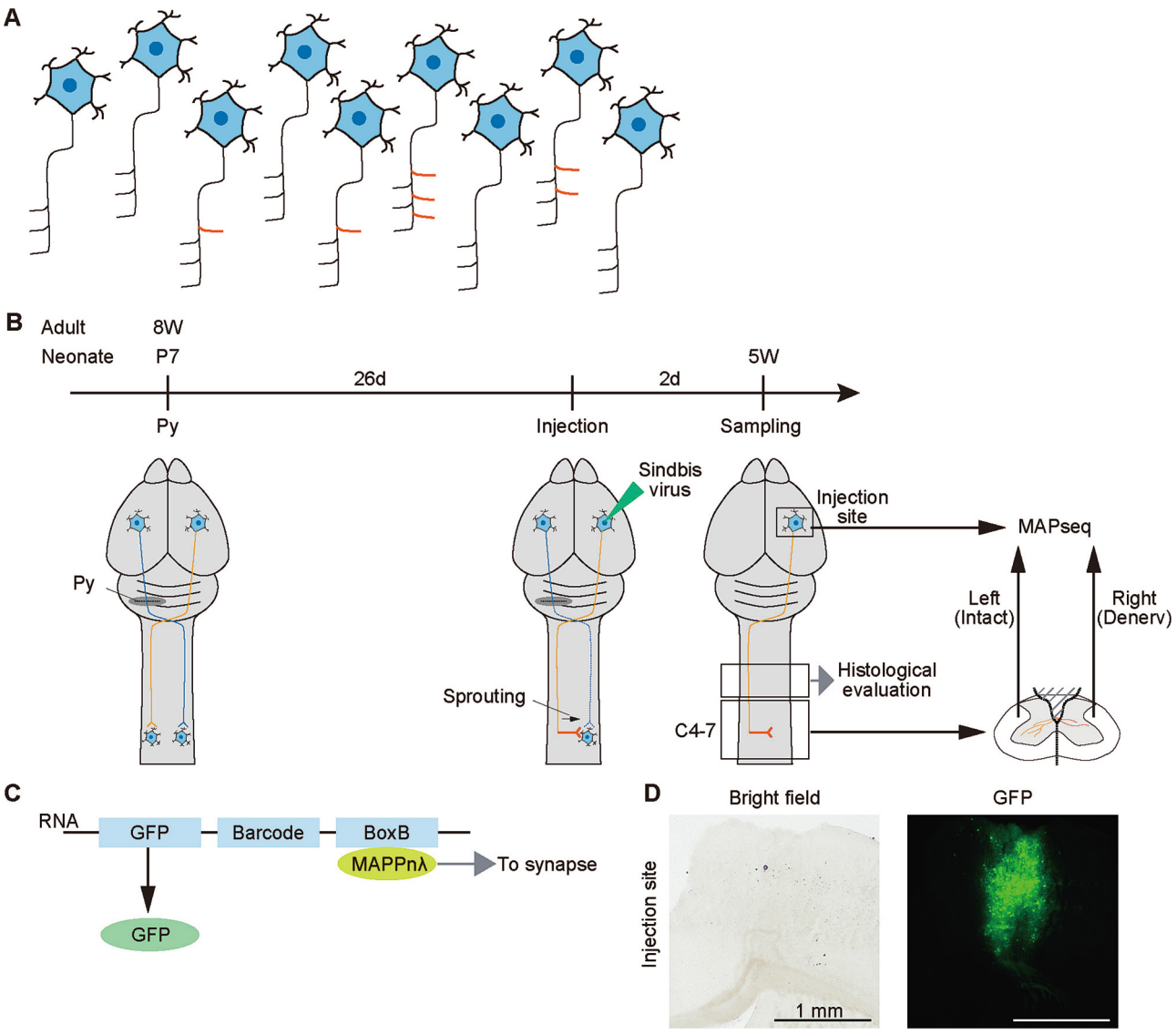

Fig. 1. Experimental design. (A) Scheme of complexity of projection pattern of sprouting neurons. Red thick lines indicate axonal sprouting. (B) Scheme of experimental design. Blue lines indicate the injured side of the corticospinal tract. Yellow lines indicate the intact side of the corticospinal tract. Py, pyramidotomy; Denerv, denervated side; W, weeks of age; P, postnatal day; d, days. (C) Scheme of subgenomic RNA derived from Sindbis virus. MAPP-nλ translated from Sindbis virus transport RNA to synapse. (D) Bright field and GFP filter images of injection site 2 days after injection. A representative image of 2 mice in neonatal group. Scale bars: 1 mm. (For interpretation of the references to colour in this figure legend, the reader is referred to the web version of this article.)

with PBS 40–44 h after injection, and ~2 mm width brain slice was fixed with 4 % PFA/0.1 M PB overnight at 4 °C for histological evaluation at the injection site. A 50-μm thickness tissue was sliced and mounted on Matsunami adhesive silane (MAS)-coated glass slide (Matsunami). The specimens were then washed with PBS and imaged using VS200 (Evident).

Alternatively, spinal cord tissue at the level of C1–3 vertebrae in the previous section was used for immunohistochemistry and RNAscope assays (Wang et al., 2012). A 14-μm thickness tissue was sliced and mounted on MAS-coated glass slide (Matsunami). For immunohistochemistry, the specimens were incubated in 400 ng/mL of anti-protein kinase C γ (PKCγ) antibody (Santa Cruz, sc-211), followed by incubation with 4 μg/mL of anti-rabbit IgG antibody conjugated with Alexa Fluor 568 (Invitrogen, A11011). For the RNAscope assay, the specimens were subjected to peroxidase inactivation, target retrieval, protease treatment, and hybridization with a GFP target probe (Advanced Cell Diagnostics, 409011) using the RNAscope Multiplex Fluorescent Kit v2 (Advanced Cell Diagnostics, 323100). The signal was amplified and developed with 1500 times dilution of Opal 690 reagent (PerkinElmer, FP1497001KT). Images were acquired using a confocal microscope FV3000 (Evident).

2.5. Data processing

Sequencing data were deposited in the DNA Data Bank of Japan (DDBJ). Cortex or C4–7 level cervical cord from an animal without injection or olfactory bulb from an animal with injection were used as negative controls. Data pre-processing was conducted at the MAPseq/BARseq Core Facility. In brief, original sequences (barcode + SSI + UMI) were sorted according to SSIs. To exclude low read molecules which may be derived from sequencing/PCR error, threshold for minimum reads were set as 2 for injection site and 10 for target sites in each brain area (SSI). Then all the barcodes whose hamming distances are no more than 3 collapsed considering the barcode length was 30 bp. At this step, the number of barcodes was 598,400 (Supplementary Table 1). Then barcodes with more than 0 UMI at the injection site and 5 UMIs in the maximum projection area were used for the analysis. At this step, the total number of barcodes was 12,786.

The following data processing was conducted using R version 4.2.0 (R Core Team, 2022) and graphs were produced using the ggplot2 package (Wickham, 2009). The counts were divided by spike-in counts, and box plots were generated. Then, the normalized counts were divided by the sum of those of all target areas (left and right cervical cords) in each mouse, as described previously (Kebschull et al., 2016a), and this value (relative projection strength) was used in the following analyses. To plot log-scale values, 10^{-5} was added to the value to avoid an infinite value. To plot the cumulative relative projection strength, the sum of the relative projection strengths of all neurons in each mouse was calculated. The sprouting index was defined as the relative projection strength on the denervated side divided by the sum of all the target sites (left and right cervical cords) in each neuron. The bin width of the histogram was as follows: (max – min)/10. A regression line was drawn using the stat_smooth function and lm method. Statistical analysis was performed using Tukey's honest significant difference (HSD) test, with a cutoff value of $P < 0.05$. For most of the analyses, all the values for each animal collapsed and analyzed. For statistical analysis relating to regression line, all the cells were combined and analyzed.

2.6. Traditional axon tracer analysis

Axon tracer analysis was performed essentially as described previously(Tsujioka and Yamashita, 2019). In brief, 600 nL of 10 % biotinylated dextran amine (BDA, Invitrogen, D1956) was injected into the right side of the motor cortex as described in Infection of Sindbis virus section at an injection speed of 200 nL/min 2 weeks after left side pyramidotomy.

The mice were perfused with 4 % PFA/0.1 M PB followed by 6 h postfixation 2 weeks after injection. C4–7 cervical cord tissues were harvested and frozen. A 20-μm thickness tissue was sliced and stained as described in immunohistochemistry section using 4 μg/mL of streptavidin conjugated with Alexa Fluor 647 (Invitrogen, S21374). Images were acquired using a confocal microscope FV3000.

A horizontal line was drawn from the central canal to the limb of the gray matter at the denervated side, and it was divided into 3 equal lengths by 2 vertical lines, Z1 and Z2, which were drawn on the gray matter. The normalized sprouting number was defined as average of the number of axons crossing a vertical line on the gray matter at the central canal (Mid), Z1 or Z2 from 5 to 6 slices/mouse, divided by average of the number of labeled main CST at the dorsal column from 3 slices. Three mice were used for each group. Statistical analysis was performed using Tukey's HSD test.

3. Results

To reveal the complexity of the projection pattern of the sprouting CST at the single-cell level in neonates and adults (Fig. 1A), we conducted MAPseq. The left side of the pyramidal tract was injured in the P7 neonates or 8 W adults, and 4 weeks after pyramidotomy, the barcoded Sindbis virus library was injected into the caudal forelimb area of the motor cortex (Fig. 1B). Two days after injection, the injection sites and the left or right side of the cervical cord (C4–7) were collected and the barcodes were sequenced. Virus infection was visualized using GFP expression (Fig. 1C), and green fluorescence was observed at the injection site (Fig. 1D).

Following the above experimental design, we collected the MAPseq samples. Starting from 5 to 10 animals, we finally used four (adult sham) or three (adult pyramidotomy, neonate sham, and neonate pyramidotomy) animals for MAPseq analysis (Table 1). We confirmed effective ablation of unilateral CST by labeling CST with anti-PKCγ antibody in ~C3 level cervical cord (Fig. 2A–L), although PKCγ signal partially remains in 1/3 samples in both adult (Fig. 2E) and neonate (Fig. 2K). We also evaluated whether the barcode RNA reached this level using RNAscope against *Gfp* mRNA (Fig. 2M–AA). Since the signal was derived from RNA in axons, the signals were observed as sparse single dots, not like GFP fluorescence signal or dense RNA signals in cell bodies. We observed several signals in the infected side of dorsal column (Fig. 2N), which may have been derived from the barcoded RNA at the main CST during transportation from cell body to the synapse. We also observed signals in the gray matter of the spinal cord in all samples (Fig. 2O–AA). Although we manually removed the dorsal column from the spinal cord sample for MAPseq analysis to remove signals derived from the main CST, the possible effect of contamination of the dorsal column might have been limited because the total signal at the dorsal column was not very high compared with that in the gray matter.

Table 1
The number of animals used in MAPseq analysis.

Age	Adult		Neonate	
Surgery	Sham	Py	Sham	Py
The animals subjected to surgery	5	7	6	10
The animals surviving at injection	5	7	5	7
The animals surviving at sample collection	5	7	4	5
Successfully collected samples	4	5	3	4
Samples with successful ablation of CST	(–)	3 (1 is partial)	(–)	3 (1 is partial)
Samples subjected to MAPseq analysis	4	3	3	3

Subsequently, MAPseq was performed. A previous MAPseq study showed that barcode counts detected at the spinal cord are approximately 1/5 of those at the brain stem (Hausmann et al., 2022), and those at the brain stem look at least 1/2 of those at the cortex after injection in the forelimb area of the motor cortex; we deemed that the expected counts in the spinal cord were approximately 1/10 of those in the strong projection target. Therefore, we set the ratio of the injection site to the target site as 10:90, which is usually set as 60:40 in the MAPseq/BARseq Core Facility. By filtering barcodes with more than 0 UMIs at the injection site and more than 5 UMIs in the maximum projection area, approximately 160–2800 barcodes were detected in each sample, except for one neonatal sham sample with no barcode (Table 2). Therefore, this sample was excluded from analysis. The GFP signal at the injection site was very weak during sample collection; therefore, the injection was probably unsuccessful. Spike-in-normalized UMI counts were prominently higher on the intact side than on the denervated side in all samples (Fig. 3A), which is consistent with the widely known fact that the major projections of the CST are to the contralateral side (intact side). To compare projection strength between mice, we calculated the relative projection strength, which was calculated as the spike-in-normalized UMI counts divided by the total value in all target areas (Fig. 3B, C). The median was near zero, and long tails extended towards higher values, indicating that few neurons projected very strongly.

Next, we plotted the relative projection strengths on the intact and denervated sides of each neuron (Fig. 4A). Neurons with high projection strengths on both sides were rare. The relative projection strength on the denervated side tended to be higher in the pyramidotomy group, especially in neonates (Fig. 4B). We plotted a graph on a log scale using the same data to clearly visualize neurons with low projection strengths (Fig. 4C). The projection strength on the denervated side was approximately one order of magnitude lower than that on the intact side. The log-scale graph more clearly shows that the projection strength tended to be higher in the neonatal pyramidotomy group (Fig. 4D, Supplementary Fig. 1). To examine the changes in the neuronal subpopulation, we calculated the ratio of neurons that projecting solely to the intact side, the denervated side, or both sides (Fig. 4E–G). For example, if relative projection strength is zero (which means UMI count is zero) in denervated side and 0.01 (more than zero) for barcode A (=neuron A), neuron A is categorized into neuronal subpopulation projecting solely to intact side. If the number of neurons categorized into neuronal subpopulation projecting solely to intact side is 100 and the number of all

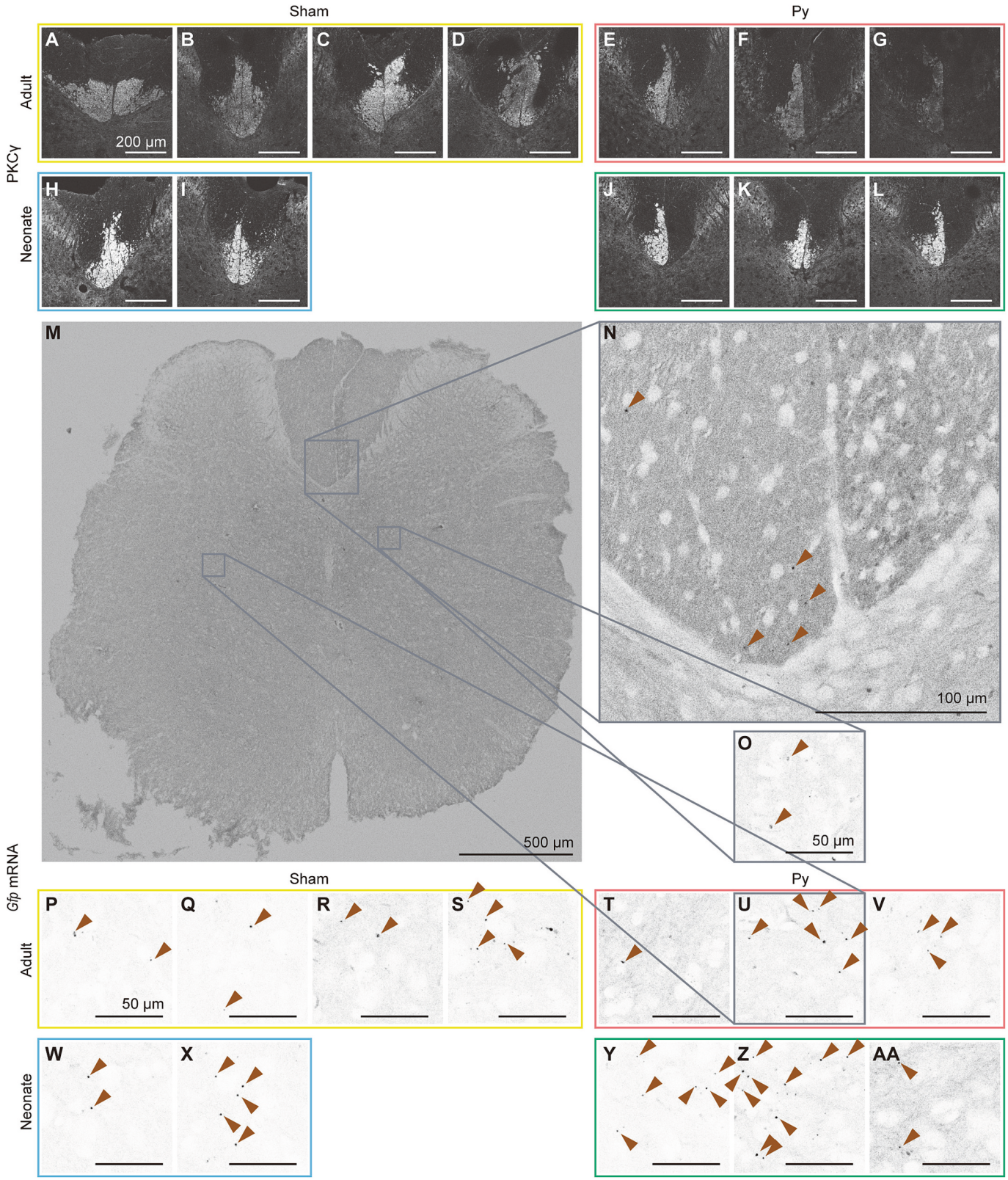

Fig. 2. Samples used in the MAPseq analysis. (A–L) Dorsal column images labeled with anti-PKCγ antibody. (M–AA) *Gfp* mRNA signals revealed via the RNAscope assay. Gray boxes in the spinal cord image (M) are enlarged in (N, dorsal column), (U, intact side of gray matter), or (O, denervated side of gray matter). Images of gray matter of the spinal cord of all samples are shown in (P-AA). Sham (A-D, H, I, P–S, W, X) or pyramidotomy group (E–G, J–O, T–V, Y–AA) injured during adult (A–G, M–V) or neonate (H–L, W–AA) are shown. Scale bars: 200 μm (A–L), 500 μm (M), 100 μm (N), or 50 μm (O–AA). Brown arrowheads indicate *Gfp* mRNA signals. The signals are indicated in white on a black background (A–L) or in black on a white background (M–AA). (For interpretation of the references to colour in this figure legend, the reader is referred to the web version of this article.)

Table 2
The number of barcodes detected.

Age	Surgery	The number of barcodes detected
Adult	Sham	163
		1824
		484
		1750
	Py	458
		553
		1632
Neonate	Sham	423
		1192
		0
	Py	591
		2834
		882

neurons detected in mouse X is 200, the cell ratio is 100/200 = 50 %. The ratio of neurons solely projecting to intact side was approximately 40–70 % and that of neurons projecting to both sides was 30–60 %. Conversely, neurons solely projecting to denervated side were very rare (approximately 0–1 %). Therefore, a mouse with high ratio of neurons solely projecting to intact side showed low ratio of neurons projecting to both sides, and vice versa. The ratio of neurons projecting solely into the intact side tended to be lower in the neonatal pyramidotomy group; however, this difference was not statistically significant.

To analyze sprouting patterns, we first compared the cumulative projection strength on the denervated side by summing the projection strengths of all neurons in each mouse (Fig. 5A). The cumulative projection strength on the denervated side was significantly higher in the neonatal pyramidotomy group than that in the other groups. This is consistent with previous studies showing that the number of sprouting axons is significantly higher in the neonatal pyramidotomy group (Liu et al., 2010), or with our confirmation of the reproducibility of the studies (Supplementary Fig. 2), supporting the validity of this analysis. We created a histogram of the relative projection strength on the denervated side in each group (Fig. 5B). Surprisingly, the distribution was almost indistinguishable between the groups, although the cumulative projection strength was very clearly different. Because more than 90 % of neurons were categorized in the lowest bin, the difference might be obscured. Therefore, to clearly visualize this difference, we plotted it on a logarithmic scale (Fig. 5C). Projection strength in the neonatal pyramidotomy group tended to be higher in broad bins at middle-to-high projection strengths, although the difference was not statistically significant (Table 3).

Finally, we analyzed another feature of sprouting neurons: the ratio of axons projecting to the denervated side among all axons of a neuron (Fig. 5D). The sprouting index was calculated as the projection strength on the denervated side divided by the total projection strength. By doing

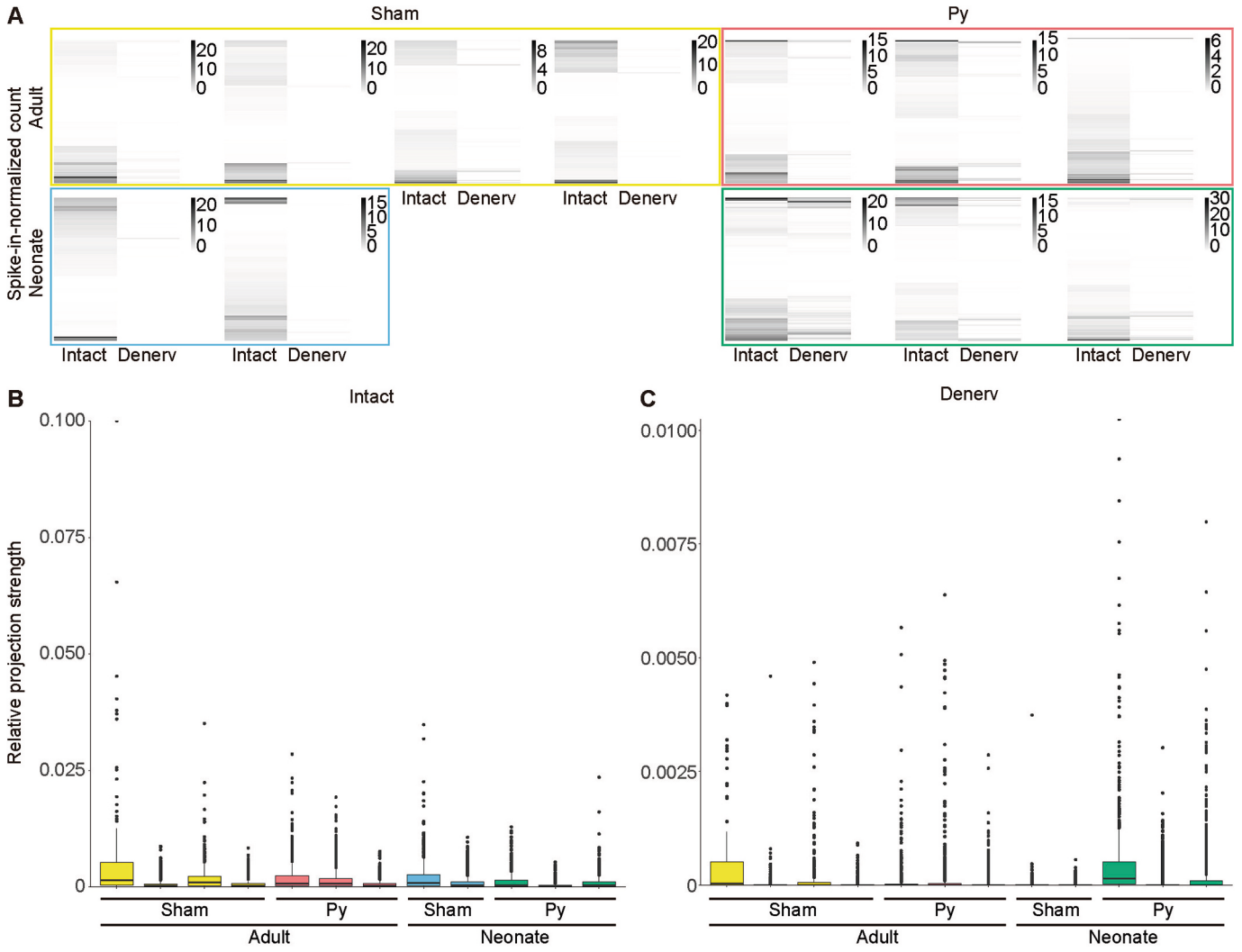

Fig. 3. MAPseq count data. (A) Spike-in-normalized count in each sample. Darker colour indicates higher counts. (B, C) Relative projection strength on the intact (B) or denervated side (C). Spike-in-normalized count is divided by the sum of that in all target areas (intact and denervated side) in each mouse.

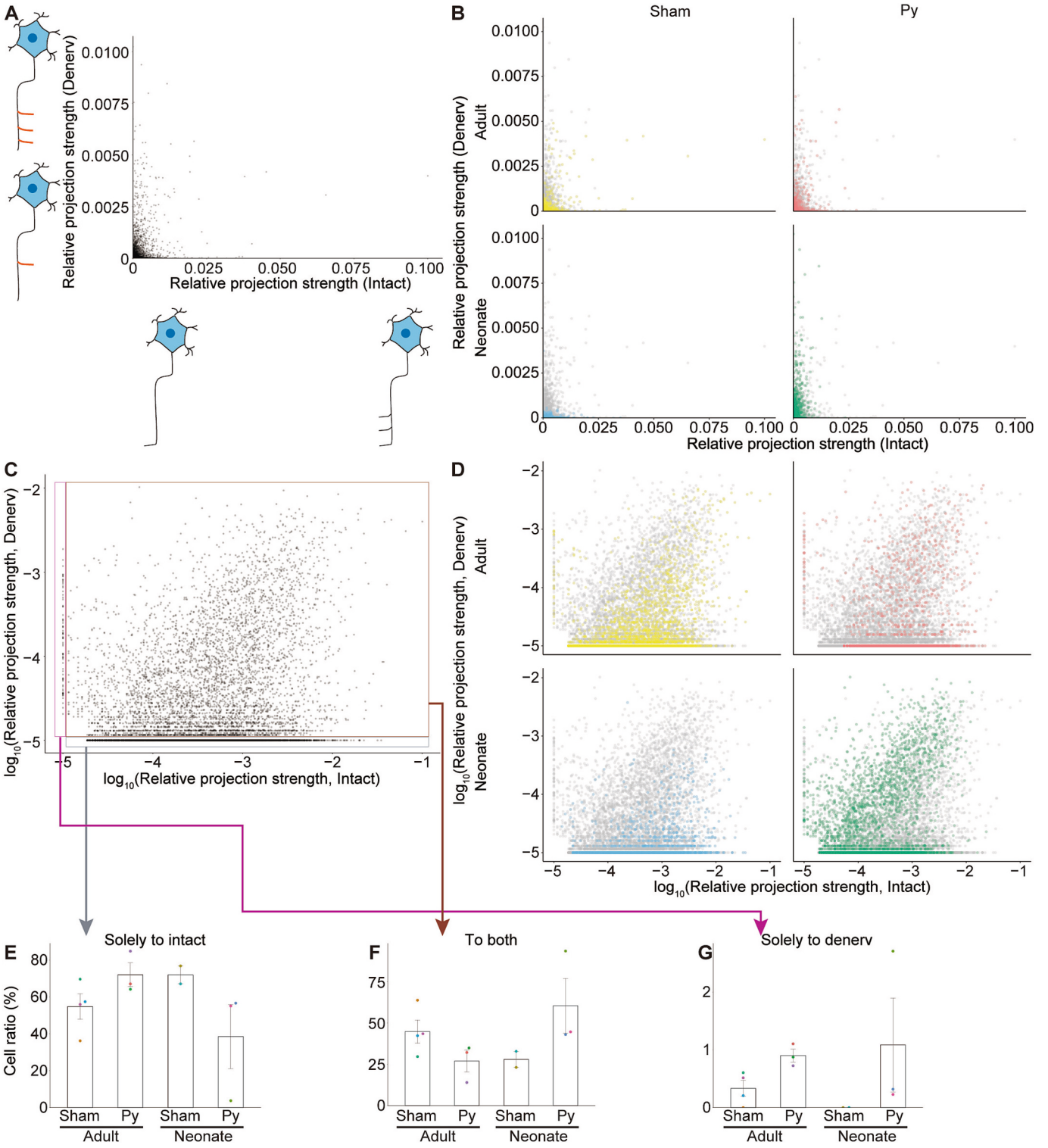

Fig. 4. Cell population revealed by MAPseq. (A–D) Scatter plot of each neuron. Horizontal axes represent relative projection strength on the intact side (A, B) or $\log_{10}$ scale of them (C, D), and vertical axes represent those in the denervated side. To avoid an infinite value, 10^{-5} is added to the relative projection strength in (C, D); therefore, the dots lined on −5 level indicate that the relative projection strengths are zero. Gray dots indicate all neurons, and adult sham (yellow), pyramidotomy (red), neonate sham (blue), or pyramidotomy (green) groups are highlighted in (B, D). (E–G) Ratio of cell population which solely project to the intact side (E, gray box in C), denervated side (G, magenta box in C), or project to both sides (F, brown box in C). Mean ± S. E. M. Different colors indicate different animals. (For interpretation of the references to colour in this figure legend, the reader is referred to the web version of this article.)

this, the range of values is limited from 0 to 1; therefore, this is probably convenient for the analysis. For example, index 0 indicates that there is no projection to the denervated side (no sprouting), 0.25 means that 1/4 of the projection is to the denervated side (sprouting side), and 0.5 means that half of the projection is to the denervated side. We examined the relationship between this value and the relative projection strength on the denervated side by drawing a graph in which the horizontal axis represents the relative projection strength on the denervated side, and

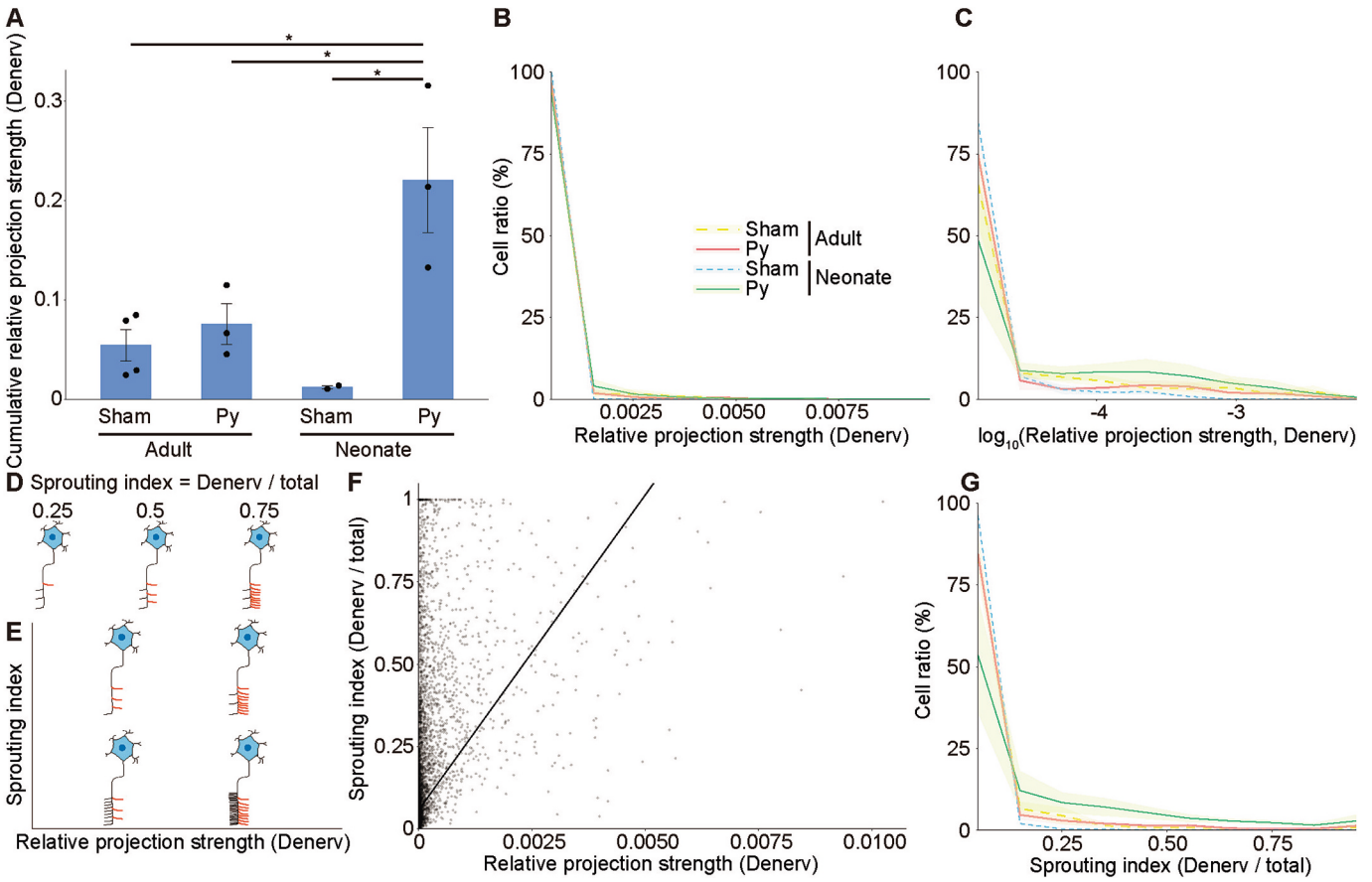

Fig. 5. Comparison of sprouting by MAPseq. (A) Cumulative relative projection strength on the denervated side. Mean ± S. E. M. * $P < 0.05$, Tukey's HSD test. (B, C) Histogram of relative projection strength. Horizontal axes represent relative projection strength (B) or $\log_{10}$ scale of them (C) and vertical axes represent cell ratio. To avoid an infinite value, 10^{-5} is added to relative projection strength in (C). (D) Scheme of sprouting index. (E) Scheme of interpretation of (F). (F) Scatter plot of relative projection strength on the denervated side and sprouting index. Regression line is inserted. (G) Histogram of sprouting index. Horizontal axis represents sprouting index and vertical axis represents cell ratio. Bin number is 10 in the histogram. Mean ± S. E. M. Thick lines indicate adult, thin lines indicate neonate, broken lines indicate sham, and solid lines indicate the pyramidotomy group.

the vertical axis represents the sprouting index (Fig. 5E). If the neurons are plotted on a diagonal line from bottom left to top right, the total projection is almost constant, and only the index differs. If the neurons are plotted on the top left, their total projection is relatively low with a high sprouting index. If neurons are plotted at the bottom right, their total projection strength is very high; therefore, projection to the denervated side is also high, even though the sprouting index is low. The result was that the regression line was from bottom left to top right with a positive intercept, and it was statistically significant ($P < 2.2 \times 10^{-16}$, $R^2 = 0.19$, $y = 1.9 \times 10^2 x + 5.7 \times 10^{-2}$; Fig. 5F), suggesting that the second and the third type of neurons are relatively rare. This also suggests that the sprouting index can be used as a surrogate marker of projection strength on the denervated side. We plotted a histogram of the sprouting index (Fig. 5G). The ratio of neurons tended to be higher in the neonatal pyramidotomy group than in all other groups in broad bins at moderate to high sprouting index; after Bonferroni adjustment, the difference was significant between the neonatal pyramidotomy group and adult sham ($P = 0.01929$) or between the neonatal pyramidotomy group and neonatal sham group ($P = 0.03705$), or almost at cutoff level ($P = 0.050673$) between the neonatal pyramidotomy group and the adult pyramidotomy group at the bin of 0.6–0.7 (Table 4), suggesting that at least the ratio of neurons projecting 2/3 of their axons by sprouting increases after pyramidotomy in neonates.

4. Discussion

In this study, we infected CSNs with the barcoded Sindbis virus and analyzed the projection patterns of individual neurons in the cervical cord after pyramidotomy in neonates and adults. We revealed that neurons solely projecting to the denervated side were very rare, and the ratio was not significantly different between the groups. We showed that the cumulative projection strength on the denervated side was significantly higher in the neonatal pyramidotomy group. We calculated the sprouting index as the projection strength on the denervated side divided by the total projection strength and showed that the sprouting index correlates with the projection strength on the denervated side. We showed that the ratio of neurons tended to be higher in broad bins at a moderate-to-high sprouting index in neonates after pyramidotomy, and the difference was significant at an index 0.6–0.7. This is the first report to show the usefulness of MAPseq in the study of axonal sprouting and the heterogeneity of sprouting patterns in neonates after pyramidotomy.

Several signals of *Gfp* RNA in the RNAscope assay were detected in the dorsal column; however, it was not prominently higher than those in the gray matter (Fig. 2M–AA). If axonal tracers such as biotinylated dextran amine were injected to label the CSNs, the signal would be prominently higher in the dorsal column than in the gray matter of the cervical cord. Probably, the barcoded RNA is transported to synapse by MAPP-nλ (Fig. 1C); therefore, RNA is enriched in synapse rather than axon. This suggests that, even if the removal of the dorsal column is incomplete, the effect is minor. The fact that MAPseq signals reflect

Table 3
Statistical test for histogram of relative projection strength on the denervated side in log scale. Tukey's HSD test was performed in each bin (*P* value) followed by Bonferroni adjustment.

Bin	Comparison	*P* value	Bonferroni adjustment
−5–−4.698934	Adult Py VS Adult Sham	0.948273	1
	Neonate Py VS Adult Py	0.523605	1
	Adult Py VS Neonate Sham	0.958656	1
	Neonate Py VS Adult Sham	0.763852	1
	Neonate Sham VS Adult Sham	0.759284	1
	Neonate Py VS Neonate Sham	0.356681	1
−4.698934–−4.397867	Adult Py VS Adult Sham	0.795527	1
	Neonate Py VS Adult Py	0.668252	1
	Adult Py VS Neonate Sham	0.970997	1
	Neonate Py VS Adult Sham	0.988237	1
	Neonate Sham VS Adult Sham	0.983666	1
	Neonate Py VS Neonate Sham	0.929044	1
−4.397867–−4.096801	Adult Py VS Adult Sham	0.341486	1
	Neonate Py VS Adult Py	0.218686	1
	Adult Py VS Neonate Sham	0.999939	1
	Neonate Py VS Adult Sham	0.957783	1
	Neonate Sham VS Adult Sham	0.410536	1
	Neonate Py VS Neonate Sham	0.274036	1
−4.096801–−3.795735	Adult Py VS Adult Sham	0.80699	1
	Neonate Py VS Adult Py	0.251889	1
	Adult Py VS Neonate Sham	0.950982	1
	Neonate Py VS Adult Sham	0.598777	1
	Neonate Sham VS Adult Sham	0.564073	1
	Neonate Py VS Neonate Sham	0.16654	1
−3.795735–−3.494669	Adult Py VS Adult Sham	0.98955	1
	Neonate Py VS Adult Py	0.596524	1
	Adult Py VS Neonate Sham	0.932184	1
	Neonate Py VS Adult Sham	0.393799	1
	Neonate Sham VS Adult Sham	0.983604	1
	Neonate Py VS Neonate Sham	0.365666	1
−3.494669–−3.193602	Adult Py VS Adult Sham	0.994766	1
	Neonate Py VS Adult Py	0.735043	1
	Adult Py VS Neonate Sham	0.814205	1
	Neonate Py VS Adult Sham	0.562246	1
	Neonate Sham VS Adult Sham	0.887068	1
	Neonate Py VS Neonate Sham	0.336443	1
−3.193602–−2.892536	Adult Py VS Adult Sham	0.940349	1
	Neonate Py VS Adult Py	0.776848	1
	Adult Py VS Neonate Sham	0.942162	1
	Neonate Py VS Adult Sham	0.965862	1
	Neonate Sham VS Adult Sham	0.708848	1
	Neonate Py VS Neonate Sham	0.526574	1
−2.892536–−2.591470	Adult Py VS Adult Sham	0.999086	1
	Neonate Py VS Adult Py	0.802098	1
	Adult Py VS Neonate Sham	0.824479	1
	Neonate Py VS Adult Sham	0.698204	1
	Neonate Sham VS Adult Sham	0.857045	1
	Neonate Py VS Neonate Sham	0.395945	1
−2.591470–−2.290403	Adult Py VS Adult Sham	0.84131	1
	Neonate Py VS Adult Py	0.969996	1
	Adult Py VS Neonate Sham	0.979551	1
	Neonate Py VS Adult Sham	0.983428	1
	Neonate Sham VS Adult Sham	0.681985	1
	Neonate Py VS Neonate Sham	0.863406	1
−2.290403–1.989337	Adult Py VS Adult Sham	0.97139	1
	Neonate Py VS Adult Py	0.490656	1
	Adult Py VS Neonate Sham	0.982772	1
	Neonate Py VS Adult Sham	0.259634	1
	Neonate Sham VS Adult Sham	1	1
	Neonate Py VS Neonate Sham	0.39021	1

synapse formation rather than axonal extension is also advantageous for many sprouting studies because synapse formation is more important for functional recovery, which is the goal of these studies.

Approximately 200–3000 barcodes were detected in each mouse (Table 2). The number is comparable to that in a previous study (Hausmann et al., 2022) in which approximately 200–300 barcodes were detected in corticospinal neurons. One of the important differences might be sampling method: MAPseq was performed after perfusion and fixation in the previous study whereas it was performed without it in this study. Fixation and staining is suitable for accurate dissection, but it affects the reverse transcription efficiency, and the barcode recovery is about 50 % of that from fresh frozen tissue (personal communication with MAPseq/BARseq Core Facility director Dr. Huiqing Zhan), therefore we chose fresh frozen tissue. However, other methods (such as injection site, collection area or thresholding criteria) are also different, therefore direct comparison is difficult. In this study, 12,786 barcodes (~2 %) were used after UMI thresholding among total 598,400 (Supplementary Table 1). Usually, the ratio of barcodes used among total barcodes is approximately 0.4–8 % (median is ~2 %) (personal

Table 4
Statistical test for histogram of sprouting index. Tukey's HSD test was performed in each bin (*P* value) followed by Bonferroni adjustment.

Bin	Comparison	*P* value	Bonferroni adjustment
0–0.1	Adult Py VS Adult Sham	0.999989	1
	Neonate Py VS Adult Py	0.206883	1
	Adult Py VS Neonate Sham	0.881053	1
	Neonate Py VS Adult Sham	0.17583	1
	Neonate Sham VS Adult Sham	0.852558	1
	Neonate Py VS Neonate Sham	0.103335	1
0.1–0.2	Adult Py VS Adult Sham	0.971071	1
	Neonate Py VS Adult Py	0.446981	1
	Adult Py VS Neonate Sham	0.956677	1
	Neonate Py VS Adult Sham	0.621022	1
	Neonate Sham VS Adult Sham	0.800635	1
	Neonate Py VS Neonate Sham	0.299789	1
0.2–0.3	Adult Py VS Adult Sham	0.96185	1
	Neonate Py VS Adult Py	0.423889	1
	Adult Py VS Neonate Sham	0.906059	1
	Neonate Py VS Adult Sham	0.617994	1
	Neonate Sham VS Adult Sham	0.684871	1
	Neonate Py VS Neonate Sham	0.228428	1
0.3–0.4	Adult Py VS Adult Sham	0.985128	1
	Neonate Py VS Adult Py	0.140976	1
	Adult Py VS Neonate Sham	0.873356	1
	Neonate Py VS Adult Sham	0.068533	0.685326
	Neonate Sham VS Adult Sham	0.959061	1
	Neonate Py VS Neonate Sham	0.070629	0.70629
0.4–0.5	Adult Py VS Adult Sham	0.980674	1
	Neonate Py VS Adult Py	0.097404	0.974037
	Adult Py VS Neonate Sham	0.87302	1
	Neonate Py VS Adult Sham	0.043962	0.43962
	Neonate Sham VS Adult Sham	0.965238	1
	Neonate Py VS Neonate Sham	0.050551	0.505513
0.5–0.6	Adult Py VS Adult Sham	0.909668	1
	Neonate Py VS Adult Py	0.254335	1
	Adult Py VS Neonate Sham	0.716663	1
	Neonate Py VS Adult Sham	0.084879	0.848791
	Neonate Sham VS Adult Sham	0.945093	1
	Neonate Py VS Neonate Sham	0.07842	0.784204
0.6–0.7	Adult Py VS Adult Sham	0.961315	1
	Neonate Py VS Adult Py	0.005067	0.050673
	Adult Py VS Neonate Sham	0.862206	1
	Neonate Py VS Adult Sham	0.001929	0.01929
	Neonate Sham VS Adult Sham	0.977433	1
	Neonate Py VS Neonate Sham	0.003705	0.037051
0.7–0.8	Adult Py VS Adult Sham	0.823949	1
	Neonate Py VS Adult Py	0.029878	0.298784
	Adult Py VS Neonate Sham	0.951943	1
	Neonate Py VS Adult Sham	0.006878	0.068784
	Neonate Sham VS Adult Sham	0.996342	1
	Neonate Py VS Neonate Sham	0.024545	0.245452
0.8–0.9	Adult Py VS Adult Sham	0.982895	1
	Neonate Py VS Adult Py	0.122795	1
	Adult Py VS Neonate Sham	0.960225	1
	Neonate Py VS Adult Sham	0.057602	0.576024
	Neonate Sham VS Adult aSham	0.997191	1
	Neonate Py VS Neonate Sham	0.090835	0.908348
0.9–1	Adult Py VS Adult Sham	0.984351	1
	Neonate Py VS Adult Py	0.661485	1
	Adult Py VS Neonate Sham	0.83364	1
	Neonate Py VS Adult Sham	0.431004	1
	Neonate Sham VS Adult Sham	0.935574	1
	Neonate Py VS Neonate Sham	0.305226	1

communication with Dr. Huiqing Zhan), therefore our result is within the normal range.

The ratio of neurons projecting to both sides was approximately 30–60 % even in sham groups (Fig. 4F). This ratio is relatively high, considering that the axonal projection to the denervated side was very rare if the CST was labeled with an axonal tracer in previous studies. One possibility is that trace amounts of contamination of intact side tissues in denervated side specimens cause an overestimation. It is likely that omitting the medial areas would produce more conservative results. However, considering that the cumulative projection strength on the denervated side replicated high sprouting in the neonatal pyramidotomy group (Fig. 5A), the overall effect was minor even if the specimen was contaminated.

Neurons with a low sprouting index and high projection strength on the denervated side (bottom right area of Fig. 5E and F) were very rare. This type of neuron has very high total projection. It is possible that the maximum axonal projection is regulated to avoid complicated signal transmission. Previous studies have identified several important factors that affect axonal sprouting after CST injury such as PTEN (Jin et al., 2015; Liu et al., 2010), suppressor of cytokine signaling 3 (Jin et al., 2015), Nogo-A (Bareyre et al., 2002; Thallmair et al., 1998), brain-derived neurotrophic factor (Ueno et al., 2012), neurotrophin-3 (Chen et al., 2008), inosine (Chen et al., 2002), or lipid phosphate phosphatase-related protein type 1 (Fink et al., 2017). It would be interesting to investigate whether intervention with these molecules increases total projections or only the sprouting index in future studies.

The ratio of neurons with a sprouting index 0.6–0.7 were very low except for the neonatal pyramidotomy group (Fig. 5G). Therefore, these neurons can be regarded as specific to neonatal sprouting. A sprouting index of 0.6–0.7 means more than half of the projection is to the denervated side; therefore, the effect on functional recovery might be higher than neurons with lower sprouting indices. Characterization of these neurons may be helpful in identifying novel therapeutic targets.

MAPseq and related techniques are very useful for connecting axonal projection patterns and other features, such as gene expression profiles, at single-cell resolution. Barcodes used in MAPseq can be identified by in situ sequencing (barcoded anatomy resolved by sequencing; BARseq) (Chen et al., 2019), and the anatomical location of the cell body of the neuron can be identified (Chen et al., 2022). The expression of dozens of genes can be visualized simultaneously (Sun et al., 2021), and neuronal subtypes specific to the projection pattern can be identified (Muñoz-Castañeda et al., 2021). MAPseq can also be combined with scRNA-seq (Klingler et al., 2021). Although infection with the Sindbis virus itself affects the gene expression profile (Uyaniker et al., 2019), these are powerful methods for unveiling gene expression in neurons with specific projection patterns. In this study, the number of neurons with a sprouting index of 0.6–0.7 in neonatal pyramidotomy group was approximately 35, which is not very low number. Therefore, the characterization of neurons with a sprouting index 0.6–0.7 might be feasible in future studies, and this might lead to finding a novel target which might be obscured in a previous bulk RNA-seq of sprouting neurons (Fink et al., 2017).

At P7, the forefront of the CST reaches a lower thoracic level (Canty and Murphy, 2008; Gianino et al., 1999; Namikawa et al., 2015), but the axonal projection pattern continues to change till 8 W (Abe et al., 2024). In our experiment, sprouting occurred from P7 to P35 (5 W) in the neonatal pyramidotomy group; therefore, the CST was still undergoing developmental changes. The high sprouting ability especially at a sprouting index 0.6–0.7 might be based on the high plasticity. It would also be interesting to investigate whether the axonal projection patterns in the neonatal pyramidotomy group changed in later stages, such as at 8 or 12 W.

During the preparation of our manuscript, we found a preprint that reported MAPseq analysis of bilaterally projecting CSNs in intact adult mice (Fait et al., 2024). Their conclusion that CSNs solely projecting to the ipsilateral side are rare among all ipsilaterally projecting neurons (solely projecting to the ipsilateral side + projecting to both sides) in the spinal cord is consistent with our conclusion (Fig. 4F, G). Our study included CST-ablated and neonatal samples, which were missing in their study. Therefore, both studies will deepen our understanding of the plasticity of CSNs.

In this study, we did not analyze the projections of the CSNs to other brain areas. A previous MAPseq study demonstrated that projections to the spinal cord in extratelencephalic neurons decrease as mice grow (Abe et al., 2024). It would be interesting to analyze the change in projection patterns in other brain areas and examine whether the

proportion of spinal cord projections changes after CST ablation in future studies.

Since injected cortex was used for MAPseq analysis, it is impossible to confirm injection site histologically in mice used for MAPseq. Therefore, we cannot strictly rule out the possibility that different brain regions were labeled only in P7 pyramidotomy group. However, statistical analysis suggests it is unlikely unless systematic error exists in P7 pyramidotomy group.

An important limitation in this study is the difficulty of comparison of different age. Since chronological age of P7 group and 8 W group (5 W and 12 W, respectively) is different, neuroanatomy in the brain, the medulla oblongata, or the spinal cord is different, which can be a confound factor. However, if we choose the same chronological age (for example, 12 W), the difference of timing after injury (11 or 4 weeks after injury) can be another confound factor. Therefore, we chose to set the same timing after injury (4 weeks) instead of same chronological age, following previous studies (Liu et al., 2010; Omoto et al., 2010). Adding analyses in the same chronological age might lead to more accurate understanding in future studies.

Another limitation in this study is high variability. The mouse with low cell ratio in solely to intact category show high cell ratio in solely to denerv category (Fig. 4E, G), suggesting some mice have very high sprouting ability, which might be a reason for the high variability. To draw strong conclusion from the highly variable data, increasing the number of animals is needed. However, the cost of MAPseq analysis is still high, therefore a reduction of the cost in the future is required. In addition to it, we performed a lot of statistical tests in Fig. 5G. Without adjustment, the chance that one bin shows a significant difference is relatively high (*P* value column in Table 4). However, to control familywise error, we performed Bonferroni adjustment (Bonferroni adjustment column in Table 4), therefore it is unlikely that the significant higher ratio of neonatal pyramidotomy group at bin 0.6–0.7 after the adjustment occurs by random chance.

CRediT authorship contribution statement

Hiroshi Tsujioka: Writing – original draft, Visualization, Validation, Methodology, Funding acquisition, Formal analysis, Data curation, Conceptualization. **Toshihide Yamashita:** Writing – review & editing, Project administration.

Funding sources

This study was supported by the Nakajima Foundation.

Declaration of competing interest

The authors declare no competing interest.

Acknowledgements

We acknowledge the MAPseq/BARseq Core Facility, Cold Spring Harbor Laboratory, for providing the Sindbis virus, sample processing, and preliminary MAPseq data acquisition.

Appendix A. Supplementary data

Supplementary data to this article can be found online at https://doi.org/10.1016/j.expneurol.2025.115386.

Data availability

MAPseq data was deposited in the DDBJ (accession number PSUB025069).

References

Abe, P., Lavalley, A., Morassut, I., Santinha, A.J., Roig-Puiggros, S., Javed, A., Klingler, E., Baumann, N., Prados, J., Platt, R.J., Jabaudon, D., 2024. Molecular programs guiding arealization of descending cortical pathways. Nature 634, 644–651. https://doi.org/10.1038/s41586-024-07895-y.

Aisaka, A., Aimi, Y., Yasuhara, O., Tooyama, I., Kimura, H., Shimada, M., 1999. Two modes of corticospinal reinnervation occur close to spinal targets following unilateral lesion of the motor cortex in neonatal hamsters. Neuroscience 90, 53–67. https://doi.org/10.1016/s0306-4522(98)00424-2.

Bareyre, F.M., Haudenschild, B., Schwab, M.E., 2002. Long-lasting sprouting and gene expression changes induced by the monoclonal antibody IN-1 in the adult spinal cord. J. Neurosci. 22, 7097–7110 https://doi.org/20026733.

Benowitz, L.I., Carmichael, S.T., 2010. Promoting axonal rewiring to improve outcome after stroke. Neurobiol. Dis. 37, 259–266. https://doi.org/10.1016/j.nbd.2009.11.009.

Cai, D., Cohen, K.B., Luo, T., Lichtman, J.W., Sanes, J.R., 2013. Improved tools for the Brainbow toolbox. Nat. Methods 10, 540–547.

Canty, A.J., Murphy, M., 2008. Molecular mechanisms of axon guidance in the developing corticospinal tract. Prog. Neurobiol. 85, 214–235. https://doi.org/10.1016/j.pneurobio.2008.02.001.

Chen, P., Goldberg, D.E., Kolb, B., Lanser, M., Benowitz, L.I., 2002. Inosine induces axonal rewiring and improves behavioral outcome after stroke. Proc. Natl. Acad. Sci. U. S. A. 99, 9031–9036. https://doi.org/10.1073/pnas.132076299.

Chen, Q., Smith, G.M., Shine, H.D., 2008. Immune activation is required for NT-3-induced axonal plasticity in chronic spinal cord injury. Exp. Neurol. 209, 497–509. https://doi.org/10.1016/j.expneurol.2007.11.025.

Chen, X., Sun, Y., Zhan, H., Huang, Z.J., Gillis, J., Zador, A.M., Chen, X., Sun, Y., Zhan, H., Kebschull, J.M., Fischer, S., Matho, K., Huang, Z.J., 2019. High-throughput mapping of long-range neuronal projection using in situ sequencing. Cell 179, 772–786.e19. https://doi.org/10.1016/j.cell.2019.09.023.

Chen, Y., Chen, X., Baserdem, B., Zhan, H., Li, Y., Davis, M.B., Kebschull, J.M., Zador, A. M., Koulakov, A.A., Albeanu, D.F., 2022. High-throughput sequencing of single neuron projections reveals spatial organization in the olfactory cortex. Cell 185, 4117–4134.e28. https://doi.org/10.1016/j.cell.2022.09.038.

Ehrengruber, M.U., Schlesinger, S., Lundstrom, K., 2011. Alphaviruses: Semliki forest virus and Sindbis virus vectors for gene transfer into neurons. Curr. Protoc. Neurosci. https://doi.org/10.1002/0471142301.ns0422s57. Chapter 4, Unit 4.22.

Fait, B.W., Cotto, B., Murakami, T.C., Hagemann-Jensen, M., Zhan, H., Freivald, C., Turbek, I., Gao, Y., Yao, Z., Way, S.W., Zeng, H., Tasic, B., Steward, O., Heintz, N., Schmidt, E.F., 2024. Spontaneously regenerative corticospinal neurons in mice. bioRxiv 1–33. https://doi.org/10.1101/2024.09.09.612115.

Fink, K.L., López-Giráldez, F., Kim, I.J., Strittmatter, S.M., Cafferty, W.B.J., 2017. Identification of intrinsic axon growth modulators for intact CNS neurons after injury. Cell Rep. 18, 2687–2701. https://doi.org/10.1016/j.celrep.2017.02.058.

Gergues, M.M., Han, K.J., Choi, H.S., Brown, B., Clausing, K.J., Turner, V.S., Vainchtein, I.D., Molofsky, A.V., Kheirbek, M.A., 2020. Circuit and molecular architecture of a ventral hippocampal network. Nat. Neurosci. 23, 1444–1452. https://doi.org/10.1038/s41593-020-0705-8.

Gianino, S., Stein, S.A., Li, H., Lu, X., Biesiada, E., Ulas, J., Xu, X.M., 1999. Postnatal growth of corticospinal axons in the spinal cord of developing mice. Brain Res. Dev. Brain Res. 112, 189–204. https://doi.org/10.1016/s0165-3806(98)00168-0.

Han, Y., Kebschull, J.M., Campbell, R.A.A., Cowan, D., Imhof, F., Zador, A.M., Mrsic-Flogel, T.D., 2018. The logic of single-cell projections from visual cortex. Nature 556, 51–56. https://doi.org/10.1038/nature26159.

Hausmann, F.S., Barrett, J.M., Martin, M.E., Zhan, H., Shepherd, G.M.G., 2022. Axonal barcode analysis of pyramidal tract projections from mouse forelimb M1 and M2. J. Neurosci. 42, 7733–7743. https://doi.org/10.1523/JNEUROSCI.1062-22.2022.

Huang, H.V., 1996. Sindbis virus vectors for expression in animal cells. Curr. Opin. Biotechnol. 7, 531–535. https://doi.org/10.1016/S0958-1669(96)80057-7.

Jin, D., Liu, Y., Sun, F., Wang, X., Liu, X., He, Z., 2015. Restoration of skilled locomotion by sprouting corticospinal axons induced by co-deletion of PTEN and SOCS3. Nat. Commun. 6, 8074. https://doi.org/10.1038/ncomms9074.

Kebschull, J.M., Garcia da Silva, P., Reid, A.P., Peikon, I.D., Albeanu, D.F., Zador, A.M., 2016a. High-throughput mapping of single-neuron projections by sequencing of barcoded RNA. Neuron 91, 975–987. https://doi.org/10.1016/j.neuron.2016.07.036.

Kebschull, J.M., Garcia da Silva, P., Zador, A.M., 2016b. A new defective helper RNA to produce recombinant Sindbis virus that infects neurons but does not propagate. Front. Neuroanat. 10, 56. https://doi.org/10.3389/fnana.2016.00056.

Klingler, E., Tomasello, U., Prados, J., Kebschull, J.M., Contestabile, A., Galiñanes, G.L., Fièvre, S., Santinha, A., Platt, R., Huber, D., Dayer, A., Bellone, C., Jabaudon, D., 2021. Temporal controls over inter-areal cortical projection neuron fate diversity. Nature 599, 453–457. https://doi.org/10.1038/s41586-021-04048-3.

Liu, K., Lu, Y., Lee, J.K., Samara, R., Willenberg, R., Sears-Kraxberger, I., Tedeschi, A., Park, K.K., Jin, D., Cai, B., Xu, B., Connolly, L., Steward, O., Zheng, B., He, Z., 2010. PTEN deletion enhances the regenerative ability of adult corticospinal neurons. Nat. Neurosci. 13, 1075–1081. https://doi.org/10.1038/nn.2603.

Livet, J., Weissman, T.a., Kang, H., Draft, R.W., Lu, J., Bennis, R.a., Sanes, J.R., Lichtman, J.W., 2007. Transgenic strategies for combinatorial expression of fluorescent proteins in the nervous system. Nature 450, 56–62. https://doi.org/10.1038/nature06293.

Mathis, V.P., Williams, M., Fillinger, C., Kenny, P.J., 2021. Networks of habenula-projecting cortical neurons regulate cocaine seeking. Sci. Adv. 7, eabj2225. https://doi.org/10.1126/sciadv.abj2225.

Muñoz-Castañeda, R., Zingg, B., Matho, K.S., Chen, X., Wang, Q., Foster, N.N., Li, A., Narasimhan, A., Hirokawa, K.E., Huo, B., Bannerjee, S., Korobkova, L., Park, C.S., Park, Y.-G., Bienkowski, M.S., Chon, U., Wheeler, D.W., Li, Xiangning, Wang, Yun, Naeemi, M., Xie, P., Liu, L., Kelly, K., An, X., Attili, S.M., Bowman, I., Bludova, A., Cetin, A., Ding, L., Drewes, R., D'Orazi, F., Elowsky, C., Fischer, S., Galbavy, W., Gao, L., Gillis, J., Groblewski, P.A., Gou, L., Hahn, J.D., Hatfield, J.T., Hintiryan, H., Huang, J.J., Kondo, H., Kuang, X., Lesnar, P., Li, Xu, Li, Y., Lin, M., Lo, D., Mizrachi, J., Mok, S., Nicovich, P.R., Palaniswamy, R., Palmer, J., Qi, X., Shen, E., Sun, Y.-C., Tao, H.W., Wakemen, W., Wang, Yimin, Yao, S., Yuan, J., Zhan, H., Zhu, M., Ng, L., Zhang, L.I., Lim, B.K., Hawrylycz, M., Gong, H., Gee, J.C., Kim, Y., Chung, K., Yang, X.W., Peng, H., Luo, Q., Mitra, P.P., Zador, A.M., Zeng, H., Ascoli, G.A., Josh Huang, Z., Osten, P., Harris, J.A., Dong, H.-W., 2021. Cellular anatomy of the mouse primary motor cortex. Nature 598, 159–166. https://doi.org/10.1038/s41586-021-03970-w.

Namikawa, T., Kikkawa, S., Inokuchi, G., Terashima, T., 2015. Postnatal development of the corticospinal tract in the reeler mouse. Kobe J. Med. Sci. 61, E71–E81.

Omoto, S., Ueno, M., Mochio, S., Takai, T., Yamashita, T., 2010. Genetic deletion of paired immunoglobulin-like receptor B does not promote axonal plasticity or functional recovery after traumatic brain injury. J. Neurosci. 30, 13045–13052. https://doi.org/10.1523/JNEUROSCI.3228-10.2010.

Omoto, S., Ueno, M., Mochio, S., Yamashita, T., 2011. Corticospinal tract fibers cross the ephrin-B3-negative part of the midline of the spinal cord after brain injury. Neurosci. Res. 69, 187–195. https://doi.org/10.1016/j.neures.2010.12.004.

R Core Team, 2022. R: A Language and Environment for Statistical Computing.

Sakaguchi, R., Leiwe, M.N., Imai, T., 2018. Bright multicolor labeling of neuronal circuits with fluorescent proteins and chemical tags. Elife 7, 1–28. https://doi.org/10.7554/eLife.40350.

Starkey, M.L., Barritt, A.W., Yip, P.K., Davies, M., Hamers, F.P.T., McMahon, S.B., Bradbury, E.J., 2005. Assessing behavioural function following a pyramidotomy lesion of the corticospinal tract in adult mice. Exp. Neurol. 195, 524–539. https://doi.org/10.1016/j.expneurol.2005.06.017.

Sun, Y.C., Chen, X., Fischer, S., Lu, S., Zhan, H., Gillis, J., Zador, A.M., 2021. Integrating barcoded neuroanatomy with spatial transcriptional profiling enables identification of gene correlates of projections. Nat. Neurosci. 24, 873–885. https://doi.org/10.1038/s41593-021-00842-4.

Thallmair, M., Metz, G.A., Z'Graggen, W.J., Raineteau, O., Kartje, G.L., Schwab, M.E., 1998. Neurite growth inhibitors restrict plasticity and functional recovery following corticospinal tract lesions. Nat. Neurosci. 1, 124–131. https://doi.org/10.1038/373.

Tsujioka, H., Yamashita, T., 2019. Comparison of gene expression profile of the spinal cord of sprouting-capable neonatal and sprouting-incapable adult mice. BMC Genomics 20, 619. https://doi.org/10.1186/s12864-019-5974-9.

Tsujioka, H., Yamashita, T., 2021. Neural circuit repair after central nervous system injury. Int. Immunol. 33, 301–309. https://doi.org/10.1093/intimm/dxaa077.

Tsujioka, H., Yamashita, T., 2023. Utilization of ethanolamine phosphate phospholyase as a unique astrocytic marker. Front. Cell. Neurosci. 17. https://doi.org/10.3389/fncel.2023.1097512.

Ueno, M., Hayano, Y., Nakagawa, H., Yamashita, T., 2012. Intraspinal rewiring of the corticospinal tract requires target-derived brain-derived neurotrophic factor and compensates lost function after brain injury. Brain 135, 1253–1267. https://doi.org/10.1093/brain/aws053.

Uyaniker, S., van der Spek, S.J.F., Reinders, N.R., Xiong, H., Li, K.W., Bossers, K., Smit, A. B., Verhaagen, J., Kessels, H.W., 2019. The effects of Sindbis viral vectors on neuronal function. Front. Cell. Neurosci. 13, 1–12. https://doi.org/10.3389/fncel.2019.00362.

Wang, F., Flanagan, J., Su, N., Wang, L.C., Bui, S., Nielson, A., Wu, X., Vo, H.T., Ma, X.J., Luo, Y., 2012. RNAscope: a novel in situ RNA analysis platform for formalin-fixed, paraffin-embedded tissues. J. Mol. Diagn. 14, 22–29. https://doi.org/10.1016/j.jmoldx.2011.08.002.

Welniarz, Q., Dusart, I., Roze, E., 2017. The corticospinal tract: evolution, development, and human disorders. Dev. Neurobiol. 77, 810–829. https://doi.org/10.1002/dneu.22455.

Wickham, H., 2009. ggplot2: Elegant Graphics for Data Analysis. Springer-Verlag, New York.

Wu, X., Zhang, Q., Gong, L., He, M., 2021. Sequencing-based high-throughput neuroanatomy: from Mapseq to Bricseq and beyond. Neurosci. Bull. 37, 746–750. https://doi.org/10.1007/s12264-021-00646-3.

Z'Graggen, W.J., Fouad, K., Raineteau, O., Metz, G.A., Schwab, M.E., Kartje, G.L., 2000. Compensatory sprouting and impulse rerouting after unilateral pyramidal tract lesion in neonatal rats. J. Neurosci. 20, 6561–6569. https://doi.org/10.1523/JNEUROSCI.20-17-06561.2000.